Numerical algorithms for solving shallow water hydro-sediment-morphodynamic equations

Citation for published version:
Borthwick, A, Xia, C, Cao, Z & Pender, G 2017, 'Numerical algorithms for solving shallow water hydro-sediment-morphodynamic equations', *Engineering Computations*, vol. 34, no. 8, pp. 2836-2861. https://doi.org/10.1108/EC-01-2016-0026

Digital Object Identifier (DOI):
10.1108/EC-01-2016-0026

Published In:
Engineering Computations

Numerical Algorithms for Solving Shallow Water Hydro-Sediment-Morphodynamic Equations

Chunchen Xia
PhD student, *State Key Laboratory of Water Resources and Hydropower Engineering Science, Wuhan University, Wuhan, China.*
Email: xcc@whu.edu.cn

Zhixian Cao
Professor, *State Key Laboratory of Water Resources and Hydropower Engineering Science, Wuhan University, Wuhan, China; and* Professor*, Institute for Infrastructure and Environment, Heriot-Watt University, Edinburgh, UK.*
Email: zxcao@whu.edu.cn

Gareth Pender
Professor, *Institute for Infrastructure and Environment, Heriot-Watt University, Edinburgh, UK; and* Guest Professor, *State Key Laboratory of Water Resources and Hydropower Engineering Science, Wuhan University, Wuhan, China.*
Email: g.pender@hw.ac.uk

Alistair G.L. Borthwick
Professor, *School of Engineering, University of Edinburgh, The King's Buildings, Edinburgh, UK; and* Guest Professor, *State Key Laboratory of Water Resources and Hydropower Engineering Science, Wuhan University, Wuhan, China.*
Email: Alistair.Borthwick@ed.ac.uk

ABSTRACT

Purpose - The purpose of this paper is to present a new numerical algorithm for solving the coupled shallow water hydro-sediment-morphodynamic equations governing fluvial processes, and also to clarify the performance of the conventional algorithm, which redistributes the variable water-sediment mixture density to the source terms of the governing equations and accordingly the hyperbolic operator is rendered similar to that of the conventional shallow water equations for clear water flows.

Design/methodology/approach - The coupled shallow water hydro-sediment-morphodynamic equations governing fluvial processes are arranged in full conservation form, and solved by a well-balanced weighted surface depth gradient method along with a slope-limited centred scheme. The present algorithm is verified for a spectrum of test cases, which involve complex flows with shock waves and sediment transport processes with contact discontinuities over irregular topographies. The conventional algorithm is evaluated as compared to the present algorithm and available experimental data.

Findings - The new algorithm performs satisfactorily over the spectrum of test cases, and the conventional algorithm is confirmed to work similarly well.

Originality/value – A new numerical algorithm, without redistributing the water-sediment mixture density, is proposed for solving the coupled shallow water hydro-sediment-morphodynamic equations. It is clarified that the conventional algorithm, involving redistribution of the water-sediment mixture density, performs similarly well. Both algorithms appear equally applicable to problems encountered in computational river modelling.

Keywords Shallow water hydro-sediment-morphodynamic equations, Well-balanced, Coupled, Finite volume method, Fluvial processes

Paper type Research paper

1. Introduction

The interactive processes of flow, sediment transport and morphological evolution influenced by both human activities and extreme natural events constitute a hierarchy of physical problems of significant interest in the fields of fluvial hydraulics and geomorphology. Great efforts have been made to establish refined numerical models and to test the models over a range of scales in laboratory and field experiments (Bellos et al. 1992, Fraccarollo and Toro 1995, Capart and Young 1998, Fraccarollo and Capart 2002, Leal et al. 2006, Spinewine and Zech 2007).

The last several decades have witnessed rapid development and widespread applications of the complete shallow water hydro-sediment-morphodynamic (SHSM) equations, which explicitly accommodate interactions between flow, sediment transport and bed evolution in a coupled manner and adopt a non-capacity sediment transport approach based on physical perspectives (Cao et al. 2004, Wu and Wang 2007). An increasing number of computational studies in hydraulic engineering and geomorphological studies are based on the SHSM equations, for example, dam-break floods over erodible bed (Cao et al. 2004, Wu and Wang 2007, Xia et al. 2010, Huang et al. 2012, Huang et al. 2014), coastal processes (Xiao et al. 2010, Kim 2015, Zhu and Dodd 2015), watershed erosion processes (Kim et al. 2013), and turbidity currents (Hu et al. 2012, Cao et al. 2015). as well as rainfall-runoff processes (Li and Duffy 2011).

The finite volume method (FVM) is one of the most promising methods for solving the SHSM equations. Pivotal to this method is the determination of the numerical flux in cases where the dependent variables may be steep-fronted or have discontinuous gradients. A series of numerical schemes are available in this regard, such as the Harten-Lax-van Leer (HLL) scheme (Harten et al. 1983, Simpson and Castelltort 2006, Wu et al. 2012), the Harten-Lax-van Leer contact wave (HLLC) scheme (Toro et al. 1994, Cao et al. 2004, Zhang and Duan 2011, Yue et al. 2015), the Roe scheme (Roe 1981, Leighton et al. 2010, Xia et al. 2010, Li and Duffy 2011), and the slope limited centred (SLIC) scheme (Toro 1999, Hu and Cao 2009, Qian et al. 2015). In recent years, well-balanced schemes have been developed to improve the handling of source terms in numerical models and extend their applications to irregular topographies.

In practice, it is usual to manipulate the original SHSM equations into a form that eliminates the variable water-sediment mixture density on the left-hand-side (LHS) of the governing equations leading to the conventional numerical algorithm (CNA) which is an extension of existing numerical schemes for shallow water equations of clear water flows (Cao et al. 2004, Simpson and Castelltort 2006, Wu and Wang 2008, Xia et al. 2010, Zhang and Duan 2011, Yue et al. 2015). However, it has so far remained poorly understood whether the equation manipulation could incur conservation errors due to the splitting of certain product derivatives by the chain rule and the reassignment of the split forms to flux gradient and source terms. Given this observation, a fully conservative numerical algorithm (FCNA) is proposed herewith to directly solve the original SHSM equations in which the mixture density is maintained on the LHS. Numerical fluxes and the bed slope source terms are estimated by the well-balanced, weighted surface depth gradient method (WSDGM) version of the SLIC scheme. The remainder of the paper is organized as follows. First, the governing equations are presented in the CNA and FCNA forms. Second, the numerical scheme used to solve the equations is outlined. Third, the CNA and FCNA are examined to show their capability of preserving quiescent flow, and then the FCNA is verified for several test cases, which involve complex flows with shock waves and also sediment transport processes with contact discontinuities over irregular topographies. Meanwhile, the CNA is also evaluated as compared to the FCNA and available experimental data. Finally, conclusions are drawn from the present work.

2. Mathematical Model

2.1 Governing equations

The governing equations of SHSM models can be derived by directly applying the Reynolds Transport Theorem in fluid dynamics (Batchelor 1967, Xie 1990), or by integrating and averaging the three-dimensional mass and momentum conservation equations (Wu 2007). For ease of description, consider longitudinally one-dimensional flow over a mobile and mild-sloped bed composed of uniform (single-sized) and non-cohesive sediment. The governing equations comprise the mass and momentum conservation equations for the water-sediment mixture flow and the mass conservation equations, respectively, for sediment and bed material. These constitute a system of four equations and four physical variables (flow depth, depth-averaged velocity, sediment concentration and bed elevation), which can be written as

$$\frac{\partial(\rho h)}{\partial t}+\frac{\partial(\rho hu)}{\partial x}=-\rho_0\frac{\partial z}{\partial t} \tag{1}$$

$$\frac{\partial(\rho hu)}{\partial t}+\frac{\partial}{\partial x}\left(\rho hu^2+\frac{1}{2}\rho gh^2\right)=\rho gh(-\frac{\partial z}{\partial x}-S_f) \tag{2}$$

$$\frac{\partial(hc)}{\partial t}+\frac{\partial(huc)}{\partial x}=E-D \tag{3}$$

$$\frac{\partial z}{\partial t}=-\frac{E-D}{1-p} \tag{4}$$

where t = time; x = streamwise coordinate; h = flow depth; u = depth-averaged flow velocity in x direction; z = bed elevation; c = flux-averaged volumetric sediment concentration; g = gravitational acceleration; $S_f=n^2u^2/h^{4/3}$ = friction slope, and n = Manning roughness; p = bed sediment porosity; E , D = sediment entrainment and deposition fluxes across the bottom boundary of flow, representing the sediment exchange between the water column and bed; $\rho=\rho_w(1-c)+\rho_s c$ = density of water-sediment mixture; $\rho_0=\rho_w p+\rho_s(1-p)$ = density of saturated bed; and ρ_w, ρ_s = densities of water and sediment. Shape factors arising from depth-averaging manipulation in the preceding equations have been presumed to be equal to unity. The empirical relations for sediment exchange between the flow and the erodible bed will be introduced according to the specific test cases in Section 3. In order to facilitate mathematical manipulation and based on the fact that the bed deformation is solely determined by the local entrainment and deposition fluxes, Eq. (4) is isolated from Eqs. (1-3) and solved separately.

2.2 Equations in traditional conservative form

In the CNA, Eqs. (1) and (2) are reformulated by eliminating the water-sediment mixture density on the LHS using the relation $\rho = \rho_w(1-c) + \rho_s c$ and Eqs. (3) and (4). Accordingly, the hyperbolic operator is rendered similar to that of the conventional shallow water equations for clear water flows, as can be seen in Eqs. (5) and (6). This treatment was first proposed and implemented by Cao et al. (2004) and has been widely used in computational river modelling (Simpson and Castelltort 2006, Wu and Wang 2007, Yue et al. 2008, Hu and Cao 2009, Xia et al. 2010, Huang et al. 2014, Li et al. 2014, Cao et al. 2015). More broadly, the idea behind this numerical strategy has also been applied to solve shallow water equations including an effective porosity parameter to represent the effect of small-scale impervious obstructions on reducing the available storage volume and effective cross section of shallow water flows (Cea and Vázquez-Cendón 2010).

$$\frac{\partial \mathbf{U}}{\partial t} + \frac{\partial \mathbf{F}}{\partial x} = \mathbf{S}_b + \mathbf{S}_f \tag{5}$$

where $\mathbf{S}_b$ = vector of bed slope source term components; $\mathbf{S}_f$ = vector of other source terms; $\mathbf{U}$ and $\mathbf{F}$ = vectors as follows,

$$\mathbf{U} = \begin{bmatrix} h \\ hu \\ hc \end{bmatrix} \qquad \mathbf{F} = \begin{bmatrix} hu \\ hu^2 + \frac{1}{2} g h^2 \\ huc \end{bmatrix} \tag{6a, b}$$

$$\mathbf{S}_b = \begin{bmatrix} 0 \\ -gh\frac{\partial z}{\partial x} \\ 0 \end{bmatrix} \quad \mathbf{S}_f = \begin{bmatrix} \left(E-D\right)/(1-p) \\ -ghS_f - \frac{(\rho_s - \rho_w) g h^2}{2\rho}\frac{\partial c}{\partial x} - \frac{(\rho_0 - \rho)(E-D)u}{\rho(1-p)} \\ E-D \end{bmatrix} \tag{6c, d}$$

2.3 Equations in new conservative form

In the FCNA, Eqs. (1)-(4) are solved directly, without first redistributing the water-sediment mixture density as in the CNA. If ρh and c/ρ are regarded as independent variables respectively, Eqs. (1)-(3) can be written in the conservative form of Eq. (5), with vectors expressed in terms of variables $\left[\rho h \quad u \quad c/\rho\right]^T$, as follows,

$$\mathbf{U} = \begin{bmatrix} \rho h \\ \rho h u \\ \rho h \frac{c}{\rho} \end{bmatrix} \qquad \mathbf{F} = \begin{bmatrix} \rho h u \\ \rho h u^2 + \frac{g}{2\rho}(\rho h)^2 \\ \rho h u \frac{c}{\rho} \end{bmatrix} \tag{7a,b}$$

$$\mathbf{S}_b = \begin{bmatrix} 0 \\ -\rho g h \frac{\partial z}{\partial x} \\ 0 \end{bmatrix} \quad \mathbf{S}_f = \begin{bmatrix} \rho_0 \left(E-D\right)/(1-p) \\ -\rho g h S_f \\ E-D \end{bmatrix} \tag{7c,d}$$

2.4 Numerical scheme

2.4.1 Finite volume discretization

Implementing the finite volume discretization along with the operator-splitting method for Eq. (5), one obtains (Aureli et al. 2008, Hu et al. 2012, Hu et al. 2015, Qian et al. 2015)

$$\mathbf{U}_i^* = \mathbf{U}_i^n - \frac{\Delta t}{\Delta x}\left(\mathbf{F}_{i+1/2}^n - \mathbf{F}_{i-1/2}^n\right) + \Delta t \mathbf{S}_{bi} \tag{8a}$$

$$\mathbf{U}_i^{n+1} = \mathbf{U}_i^* + \Delta t \mathbf{S}_f^{RK} \tag{8b}$$

where Δt = time step; Δx = spatial step; i = spatial node index; n = time node index; $\mathbf{F}_{i+1/2}$ = inter-cell numerical flux at $x = x_{i+1/2}$; and the source term $\mathbf{S}_f^{RK}$ is solved by the third-order Runge-Kutta (RK) method (Gottlieb and Shu 1998)

$$\mathbf{S}_f^{RK} = \frac{1}{6}\left[\mathbf{S}_f\left(\mathbf{U}_i^{*1}\right) + 4\mathbf{S}_f\left(\mathbf{U}_i^{*2}\right) + \mathbf{S}_f\left(\mathbf{U}_i^{*3}\right)\right] \tag{9}$$

$$\mathbf{U}_i^{*1} = \mathbf{U}_i^* \tag{10a}$$

$$\mathbf{U}_i^{*2} = \mathbf{U}_i^{*1} + \frac{\Delta t}{2}\mathbf{S}_f\left(\mathbf{U}_i^{*1}\right) \tag{10b}$$

$$\mathbf{U}_i^{*3} = 2\left[\mathbf{U}_i^{*1} + \Delta t \mathbf{S}_f\left(\mathbf{U}_i^{*2}\right)\right] - \left[\mathbf{U}_i^{*1} + \Delta t \mathbf{S}_f\left(\mathbf{U}_i^{*1}\right)\right] \tag{10c}$$

The bed deformation is updated by the discretization of Eq. (4)

$$z_i^{n+1} = z_i^n + \Delta t \frac{\left(D - E\right)_i^{RK}}{\left(1 - p\right)} \tag{11}$$

For numerical stability, the time step satisfies the Courant–Friedrichs–Lewy (CFL) condition

$$\Delta t = \frac{C_r}{\lambda_{\max} / \Delta x} \tag{12}$$

where C_r is the Courant number and $C_r < 1$; and $\lambda_{\max}$ is the maximum celerity computed from the Jacobian matrix $\partial \mathbf{F} / \partial \mathbf{U}$.

2.4.2 Well-balanced version of the SLIC scheme

Unlike certain well-balanced numerical schemes which directly adopt the water surface elevation as a flow variable in their rearranged SHSM equations (Rogers et al. 2003, Liang and Borthwick

2009, Liang and Marche 2009, Huang et al. 2012, Huang et al. 2014, Qian et al. 2015), the present model maintains the original equations, with the water depth variable evaluated from a weighted average of the slope limited water depth and water surface elevation (Zhou et al. 2001, Aureli et al. 2008, Hu et al. 2012) in the framework of the SLIC scheme that results from replacing the Godunov flux by the FORCE flux in the MUSCL-Hancock scheme (Toro 2001). The original SLIC scheme (Toro 2001, Aureli et al. 2004) is termed a depth-gradient method (DGM) version because it uses the spatial gradient of the water depth for the interpolation, and is robust and stable for cases involving high gradient in water level provided the bathymetry has small gradient. The scheme is also capable of tracking the motion of wetting and drying fronts above a threshold flow depth $h_{\lim}$ as discussed in Section 2.4.3. However, when the bed topography is irregular and has large spatial gradient, the DGM version may not reproduce the exact solution for stationary flows (i.e., it does not satisfy the exact *C-property* (Bermudez and Vazquez 1994)) because of the imbalance between the bed slope source term and flux gradient. The *C-property* can be instead satisfied by the surface gradient method (SGM) proposed by Zhou et al. (2001), which is preferable for cases when small gradient in water level occurs alongside high gradient in water depth. However this method still has certain limitations in the treatment of the wetting and drying fronts that may lead to unphysical results (Aureli et al. 2008). To exploit the advantages of both DGM and SGM, the well-balanced WSDGM version of the SLIC scheme has been put forward by Aureli et al. (2008), and is employed herein to estimate the numerical fluxes as well as the bed slope source term in Eq. (8a). This method involves following three steps (Aureli et al. 2008, Hu et al. 2015). Figure 1 provides a definition sketch.

Step 1: Data reconstruction

For ease of description, a new vector of dependent variables $\mathbf{Q}$ is introduced, with $\mathbf{Q}_{TNA} = \begin{bmatrix} h & hu & hc & h+z & z \end{bmatrix}^T$ and $\mathbf{Q}_{NNA} = \begin{bmatrix} \rho h & \rho hu & \rho h \dfrac{c}{\rho} & \rho h + \rho z & \rho z \end{bmatrix}^T$ indicating the conventional and fully conservative algorithms respectively. The first four boundary extrapolated variables $\mathbf{Q}_{i+1/2}^{L}$ and $\mathbf{Q}_{i+1/2}^{R}$ are evaluated at the left and right sides of interface $x = x_{i+1/2}$ to achieve second-order accuracy in space.

$$\mathbf{Q}_{i+1/2}^{L} = \mathbf{Q}_{i}^{n} + \varphi_{i-1/2}^{L} \frac{\mathbf{Q}_{i}^{n} - \mathbf{Q}_{i-1}^{n}}{2} \tag{13a}$$

$$\mathbf{Q}_{i+1/2}^{R} = \mathbf{Q}_{i+1}^{n} - \varphi_{i+3/2}^{R} \frac{\mathbf{Q}_{i+2}^{n} - \mathbf{Q}_{i+1}^{n}}{2} \tag{13b}$$

where φ = slope limiter, which is a function of the ratios $r^{L,R}$ of variables $\mathbf{Q}$. Here the Minmod limiter is used, which reads

$$\varphi(r) = \begin{cases} \min(r,1) & \text{if } r>0 \\ 0 & \text{if } r \le 0 \end{cases} \tag{14}$$

with

$$r_{i-1/2}^{L} = \frac{Q_{i+1}^{n} - Q_{i}^{n}}{Q_{i}^{n} - Q_{i-1}^{n}} \qquad r_{i+3/2}^{R} = \frac{Q_{i+1}^{n} - Q_{i}^{n}}{Q_{i+2}^{n} - Q_{i+1}^{n}} \tag{15a, b}$$

The last elements of $\mathbf{Q}_{i+1/2}^{L}$ and $\mathbf{Q}_{i+1/2}^{R}$ are evaluated at the interface $x = x_{i+1/2}$, such that,

$$\mathbf{Q}_{i+1/2}^{L}(5) = \mathbf{Q}_{i+1/2}^{R}(5) = \frac{1}{2}\left(\mathbf{Q}_{i}^{n}(5) + \mathbf{Q}_{i+1}^{n}(5)\right) \tag{16}$$

The first elements of $\mathbf{Q}_{i+1/2}^{L}$ and $\mathbf{Q}_{i+1/2}^{R}$ are updated by a weighted average of boundary extrapolated values derived from MUSCL DGM and SGM extrapolations as follows:

$$\mathbf{Q}_{i+1/2}^{L}(1) = \phi\mathbf{Q}_{i+1/2}^{L}(1) + (1-\phi)\left[\mathbf{Q}_{i+1/2}^{L}(4) - \mathbf{Q}_{i+1/2}^{L}(5)\right] \tag{17a}$$

$$\mathbf{Q}_{i+1/2}^{R}(1) = \phi\mathbf{Q}_{i+1/2}^{R}(1) + (1-\phi)\left[\mathbf{Q}_{i+1/2}^{R}(4) - \mathbf{Q}_{i+1/2}^{R}(5)\right] \tag{17b}$$

where ϕ = weighting factor between the DGM and SGM with $0 \le \phi \le 1$, which is specified as a function of the Froude number,

$$\phi = \begin{cases} 0.5\left[1-\cos\left(\dfrac{\pi Fr}{Fr_{\lim}}\right)\right] & 0 \le Fr \le Fr_{\lim} \\ 1 & Fr > Fr_{\lim} \end{cases} \tag{18}$$

where $Fr_{\lim}$ is an upper limit beyond which a pure DGM reconstruction is performed. In this paper, $Fr_{\lim} = 2.0$ is adopted according to Aureli et al. (2008).

Boundary extrapolated vectors $\mathbf{Q}_{i+1/2}^{L}$ and $\mathbf{Q}_{i+1/2}^{R}$ are used to update the vectors of conserved variables of the governing equations as follows

$$\mathbf{U}_{i+1/2}^{L} = \left[\mathbf{Q}_{i+1/2}^{L}(1) \quad \mathbf{Q}_{i+1/2}^{L}(2) \quad \mathbf{Q}_{i+1/2}^{L}(3)\right]^{T} \tag{19a}$$

$$\mathbf{U}_{i+1/2}^{R} = \left[\mathbf{Q}_{i+1/2}^{R}(1) \quad \mathbf{Q}_{i+1/2}^{R}(2) \quad \mathbf{Q}_{i+1/2}^{R}(3)\right]^{T} \tag{19b}$$

Step 2: Evolution of extrapolated variables

The boundary extrapolated conserved variables are further evolved over $\Delta t/2$ to achieve second-order accuracy in time. In order to satisfy the *C-property* when WSDGM is adopted, the contribution due to gravity must be included

$$\bar{\mathbf{U}}_{i+1/2}^{L} = \mathbf{U}_{i+1/2}^{L} - \frac{\Delta t/2}{\Delta x}\left[\mathbf{F}(\mathbf{U}_{i+1/2}^{L}) - \mathbf{F}(\mathbf{U}_{i-1/2}^{R})\right] + \frac{\Delta t}{2}\mathbf{S}_{bi} \tag{20a}$$

$$\bar{\mathbf{U}}_{i+1/2}^{R} = \mathbf{U}_{i+1/2}^{R} - \frac{\Delta t/2}{\Delta x}\left[\mathbf{F}(\mathbf{U}_{i+3/2}^{L}) - \mathbf{F}(\mathbf{U}_{i+1/2}^{R})\right] + \frac{\Delta t}{2}\mathbf{S}_{bi+1} \tag{20b}$$

where $\mathbf{S}_{bi}$ in Eqs. (20a) and (20b) are discretized using central-differences with extrapolated variables taken from Step 1 and $z_{i+1/2} = (z_{i+1} + z_i)/2$.

$$\mathbf{S}_{bi} = \begin{bmatrix} 0 \\ -g\left[\mathbf{U}_{i+1/2}^{L}(1) + \mathbf{U}_{i-1/2}^{R}(1)\right](z_{i+1/2} - z_{i-1/2})/(2\Delta x) \\ 0 \end{bmatrix} \tag{21}$$

Step 3: Numerical fluxes and bed slope source term

The numerical fluxes are estimated by the FORCE (first-order centred) approximate Riemann solver, which is an average of the Lax–Friedrichs flux $\mathbf{F}^{LF}$ and the two-step Lax–Wendroff flux $\mathbf{F}^{LW2}$ (Toro 2001)

$$\mathbf{F}_{i+1/2} = \left(\mathbf{F}_{i+1/2}^{LW2} + \mathbf{F}_{i+1/2}^{LF}\right)/2 \tag{22}$$

$$\mathbf{F}_{i+1/2}^{LW2} = \mathbf{F}(\mathbf{U}_{i+1/2}^{LW2}) \tag{23a}$$

$$\mathbf{U}_{i+1/2}^{LW2} = \frac{1}{2}\left(\bar{\mathbf{U}}_{i+1/2}^{R} + \bar{\mathbf{U}}_{i+1/2}^{L}\right) - \frac{1}{2}\frac{\Delta t}{\Delta x}\left(\mathbf{F}\left(\bar{\mathbf{U}}_{i+1/2}^{R}\right) - \mathbf{F}\left(\bar{\mathbf{U}}_{i+1/2}^{L}\right)\right) \tag{23b}$$

$$\mathbf{F}_{i+1/2}^{LF} = \frac{1}{2}\left(\mathbf{F}\left(\bar{\mathbf{U}}_{i+1/2}^{R}\right) + \mathbf{F}\left(\bar{\mathbf{U}}_{i+1/2}^{L}\right)\right) - \frac{1}{2}\frac{\Delta x}{\Delta t}\left(\bar{\mathbf{U}}_{i+1/2}^{R} - \bar{\mathbf{U}}_{i+1/2}^{L}\right) \tag{24}$$

Finally, the bed slope source term in Eq. (8a) is computed using the evolved variables from Step 2,

$$\mathbf{S}_{bi} = \begin{bmatrix} 0 \\ -g\left[\bar{\mathbf{U}}_{i+1/2}^{L}(1) + \bar{\mathbf{U}}_{i-1/2}^{R}(1)\right](z_{i+1/2} - z_{i-1/2})/(2\Delta x) \\ 0 \end{bmatrix} \tag{25}$$

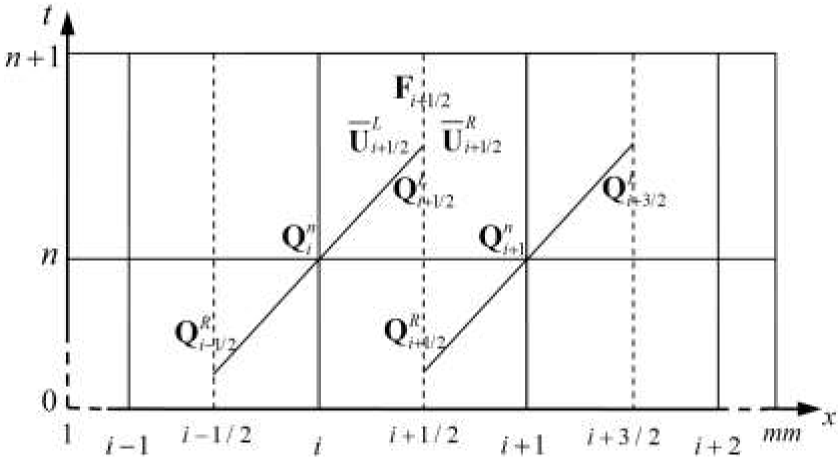

Figure 1. Sketch of the WSDGM version of the SLIC scheme

2.4.3 Wet/dry front

In order to satisfy the *C-property*, a special treatment is performed at a wet-dry front. A threshold flow depth $h_{\lim}$ is used to judge whether the cell is dry or wet. Two neighboring cells will be defined as the wet/dry front if one is wet and the other is dry. If the water surface of the wet cell is lower than the bed elevation of its adjacent dry cell, the bed elevation and water surface of the dry cell are set to be the water level of the wet cell and, consequently, the water depth is zero when computing the numerical flux. The threshold flow depth $h_{\lim}$ is a model parameter and should be sufficiently small for quantitative accuracy. A value of $h_{\lim} = 1\times10^{-6}$ is adopted in the present work.

3. Test Cases

A series of test cases is presented to verify the performance of the FCNA, accompanied by comparisons with the CNA using the same numerical scheme. The test cases include steady flow at equilibrium conditions over a steep bump (Aureli et al. 2008) (Case 1) to examine satisfaction of the *C-property*, a density dam break with a single and two initial discontinuities without bed deformation (Leighton et al. 2010) (Cases 2 and 3), dam-break over erodible beds at prototype-scale (Cao et al. 2004) (Case 4) and laboratory-scale (Fraccarollo and Capart 2002) (Case 5), and a reproduction of a large-scale flume experiment of landslide dam failure (Cao et al. 2011a) (Case 6). The spatial step Δx is set specifically for different cases and the time step Δt then obtained according to the CFL stability requirement of Eq. (12), as listed in Table I. In Case 5, the flow depth temporal and spatial scales are so small that a relatively large frictional source term may lead to numerical instability even if the CFL condition is satisfied. Thus a sub-time step Δt_σ is deployed when updating the solutions to the next time step in Eq. (8b) of Case 5, following Qian et al. (2015). It should be noted that the maximum sub-time step Δt_s in Qian et al. (2015) was derived for the second-order R-K method. For the third-order R-K method (Gear 1971) used herein, the maximum sub-time step is similarly derived, giving $\Delta t_s = 2.51h^{4/3} / gn^2u$. Table II summarizes the parameter values for the different test cases.

Table I. Spatial increment and Courant number used in test cases

Test case	1	2	3	4	5	6
Spatial step Δx (m)	0.05	0.02	0.02	10	0.005	0.04
Courant number C_r	0.95	0.95	0.95	0.95	0.95	0.95

Table II. Summary of test cases

Test case	Sediment density ρ_s (kg/m^3)	Water density ρ_w (kg/m^3)	Gravitational acceleration g (m/s^2)	Sediment diameter d (mm)	Manning roughness n	Sediment porosity p
1	2,650	1,000	9.8	N/A	0.0	N/A
2	10.0	1.0	1.0	N/A	0.0	N/A
3	0.5&2.0	1.0	1.0	N/A	0.0	N/A
4	2,650	1,000	9.8	8.0	0.03	0.4
5*	1,540	1,000	9.8	3.5	0.025	0.3
6*	2,650	1,000	9.8	0.8	0.012	0.4

Notes: * Cases using measured data.

To quantify the differences between FCNA and CNA, as well as the discrepancies between the simulations and available experiment data, the non-dimensional discrepancy is defined based on the L^1 norm.

$$L_{hz} = \frac{\sum abs\left[(h+z)_{TNA_i} - (h+z)_{NNA_i}\right]}{\sum abs\left[(h+z)_{TNA_i}\right]} \times 100\% \tag{26a}$$

$$L_z = \frac{\sum abs\left(z_{TNA_i} - z_{NNA_i}\right)}{\sum abs\left(z_{TNA_i}\right)} \times 100\% \tag{26b}$$

$$L_u = \frac{\sum abs\left(u_{TNA_i} - u_{NNA_i}\right)}{\sum abs\left(u_{TNA_i}\right)} \times 100\% \tag{26c}$$

$$L_c = \frac{\sum abs\left(c_{TNA_i} - c_{NNA_i}\right)}{\sum abs(c_{TNA_i})} \times 100\% \qquad (26d)$$

$$L_{hz}^{*} = \frac{\sum abs\left[(h+z)_i - (h+z)_{*i}\right]}{\sum abs\left[(h+z)_{*i}\right]} \times 100\% \qquad (27)$$

where L_{hz}, L_z, L_u and L_c are the L^1 norms for stage, bed elevation, velocity and concentration used to compare FCNA with CNA. L_{hz}^{*} is the L^1 norm for stage used to compare the predictions by FCNA and CNA with measured data for Cases 5 and 6. Also, $h+z$, z, u and c are the predicted stage, bed elevation, velocity and concentration with subscripts FCNA and CNA denoting corresponding algorithms whilst $(h+z)_*$ and z_* are measured stage and bed elevation.

3.1 Cases 1a and 1b: Steady flow at rest over a steep bump

To test whether or not the numerical algorithms satisfy the *C-property* over irregular topography, a $[-10 \text{ m} \le x \le 10 \text{ m}]$ frictionless channel is considered with its bed profile characterized by the presence of a steep bump, described as (Liska and Wendroff 1998)

$$z(x) = \begin{cases} 0.8\left(1 - x^2/4\right) & -2 \text{ m} \le x \le 2 \text{ m} \\ 0 & \text{elsewhere} \end{cases} \qquad (28)$$

Initially the flow is static and there is no water or sediment input at the inlet boundary. Two conditions of initial stage are considered. One is at the stage of 1.0 m (i.e., wet bed application), and the other is at the stage of 0.5 m (i.e., with wet-dry interfaces).

Figures 2 and 3 show the predicted stage and depth-averaged velocity profiles over the subdomain $[-3 \text{ m} \le x \le 3\text{m}]$ at time $t = 1$ h obtained for the two initial stage conditions, using the FCNA and CNA. The initial steady, static equilibrium state is maintained by both algorithms, demonstrating that they are exactly well-balanced for cases with irregular topography irrespective of whether or not wet-dry interfaces are involved.

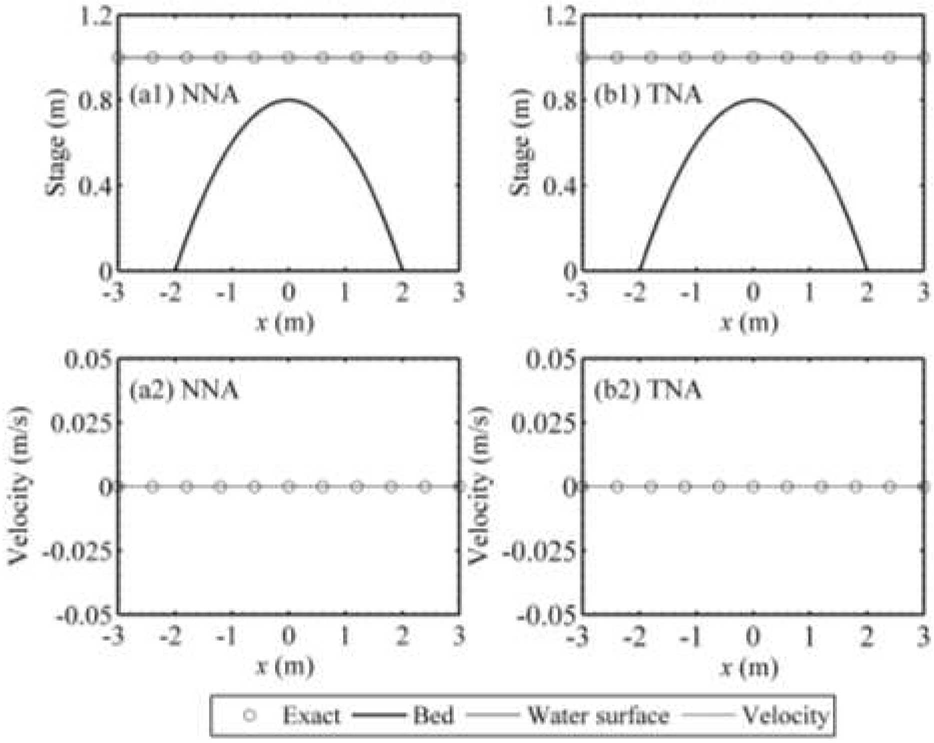

Figure 2. Case 1a: equilibrium stage and velocity profiles predicted by FCNA and CNA for initial stage of 1.0 m

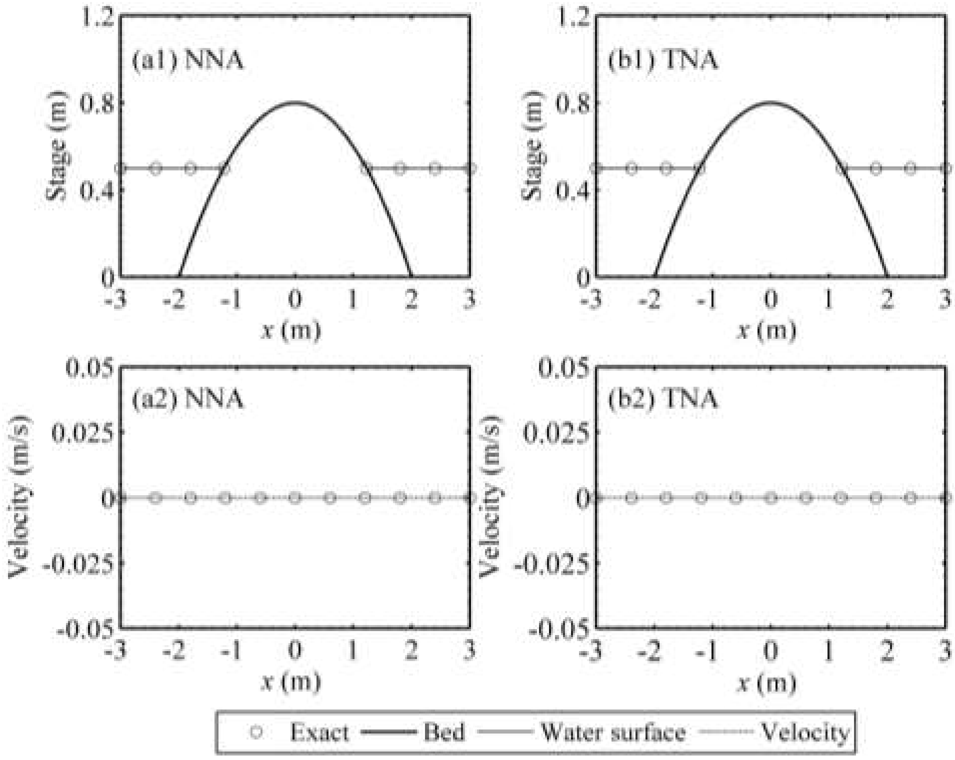

Figure 3. Case 1b: equilibrium stage and velocity profiles predicted by FCNA and CNA for initial stage of 0.5 m

3.2 Case 2: Density dam break with a single discontinuity

Attention is now focused on the initial and intermediate period following a dam break caused by two adjacent liquids of different densities but equal initial stage. The horizontal and fixed channel length is set to be L = 500 m, and the dam is located at the middle of the channel (x = 250 m). Initially, the liquids in the channel are at rest with the same stage of 1 m, and the densities to the left and right of the dam are ρ_L = 10 kg/m^3 (concentration c_L = 1) and ρ_R = 1 kg/m^3 (concentration c_R = 0), respectively.

Figure 4 shows the similarity between the stage, velocity and concentration profiles computed by the FCNA and CNA at times t = 30 and 100 s. Figure 5 compares the predicted stage, velocity and concentration time histories at sections x = 225 and 275 m (i.e. 25 m upstream and downstream of the dam respectively), which indicate that the differences in results between the two algorithms are trivial. Quantitatively, the values of L_{hz}, L_u and L_c are provided to highlight the detailed differences between the FCNA and CNA, as given in Table III. It can be seen that the values are almost the same at x = 225 m and increase a little but remain within 3% at x =275 m. Meanwhile, the values of L_{hz}, L_u and L_c at selected instants are within 1%, 3% and 0.5% respectively, which demonstrate close agreement between the simulations produced by the two algorithms.

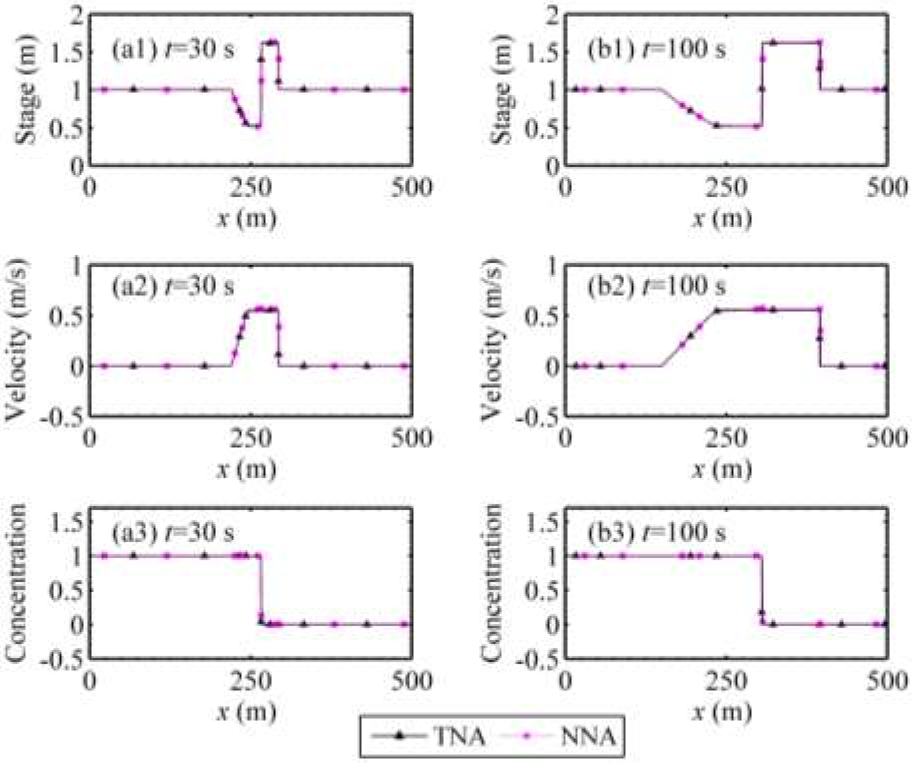

Figure 4. Case 2: stage and velocity profiles predicted by FCNA and CNA for density dam break with a single discontinuity at times: (a) t = 30 s; and (b) t = 100s.

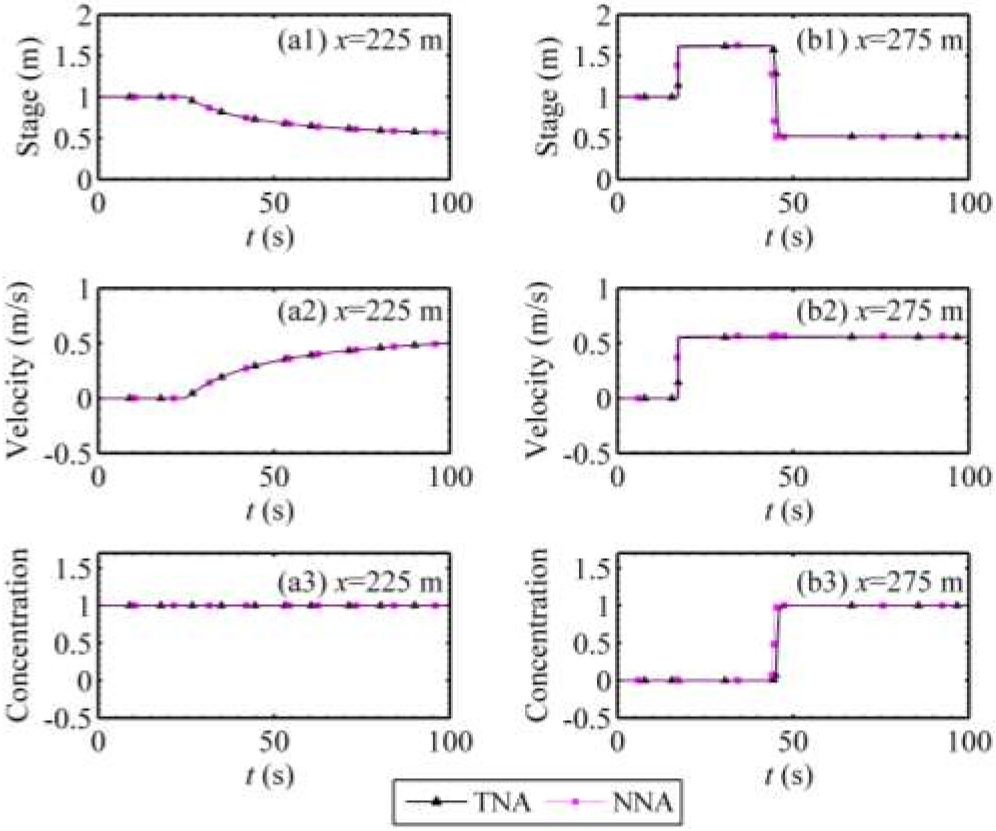

Figure 5. Case 2: stage and velocity time histories predicted by FCNA and CNA for density dam break with a single discontinuity at locations: (a) x = 225 m; and (b) x = 275 m.

Table III. L_{hz}, L_u and L_c for Case 2

Location or Time	$x = 225$ m	$x = 275$ m	$t = 30$ s	$t = 100$ s
L_{hz} (%)	0.01	2.24	0.30	0.68
L_u (%)	0.02	2.07	2.92	1.95
L_c (%)	0.00	1.93	0.17	0.33

3.3 Cases 3a and 3b: Density dam break with two initial discontinuities

Case 3 considers a density dam break in a channel with fixed horizontal bed, containing a central region of different density to that elsewhere in the channel. The channel is 100 m long and the region of different density is 1 m wide separated by two infinitesimally thin dams located at x = 249.5 and x = 250.5 m. Initially, the stage throughout the channel is 1 m, and the liquid densities in the central region bounded by the dam walls are ρ_{in} = 0.5 (Case 3a) and 2 kg/m^3 (Case 3b) with the initial interior concentration set to c_{in} = 1. Elsewhere the initial liquid density is set to ρ_{out} = 1 kg/m^3 with initial concentration $c_{out} = 0$.

Figures 6 and 7 show the stage, velocity, and concentration profiles for ρ_{in} = 0.5 and 2 kg/m^3 respectively, computed by FCNA and CNA. Figures 8 and 9 show the corresponding temporal variations in stage, velocity and concentration at x = 25, 50 and 75 m (i.e. upstream of the first dam, at the mid-point between the dams, and downstream of the second dam). The predicted interactions between the denser liquid and less dense liquid by FCNA and CNA are almost identical: the denser liquid moves inwards towards the centre of the channel, squeezing the less dense region upwards for ρ_{in} = 0.5 kg/m^3, whilst for ρ_{in} = 2 kg/m^3, the denser liquid falls under gravity, driving left and right shock-type bores into the adjacent less dense liquid. Computed profiles of the temporal variations at selected sections for ρ_{in} = 0.5 and 2 kg/m^3 show opposite behaviour in water surface and velocity (Figs. 8 and 9) because the relative density ρ_{in} / ρ_{out} is less and greater than 1.0 respectively. Tables IV and V list the values obtained for L_{hz}, L_u and L_c for Cases 3a and 3b. L_{hz} has values close to zero, indicating negligible discrepancies between the two algorithms at the selected sections and instants. The L_u and L_c values are within 4%, a limited discrepancy. Case 2 and Case 3 confirm that both FCNA and CNA provide acceptable solutions to the problems of dam break arising from discontinuous density gradients.

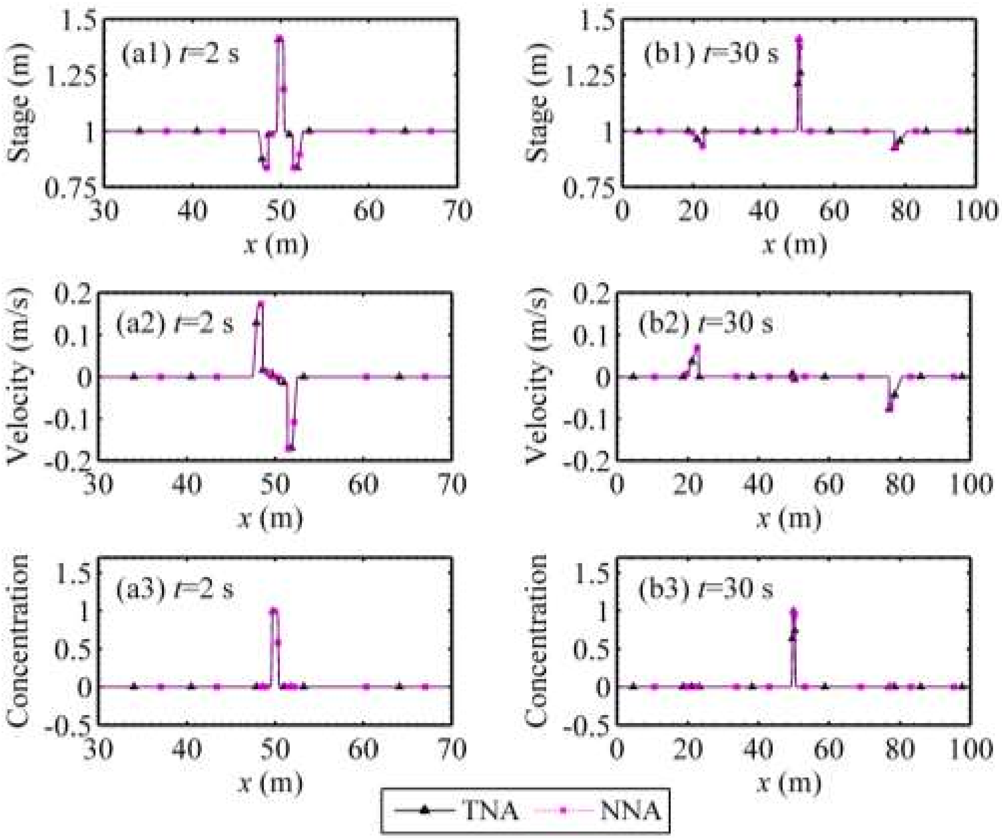

Figure 6. Case 3a: stage, velocity, and concentration profiles at times (a) t = 2 s and (b) t = 30 s, predicted by FCNA and CNA for density dam break (ρ_{in} = 0.5 kg/m^3) with two discontinuities.

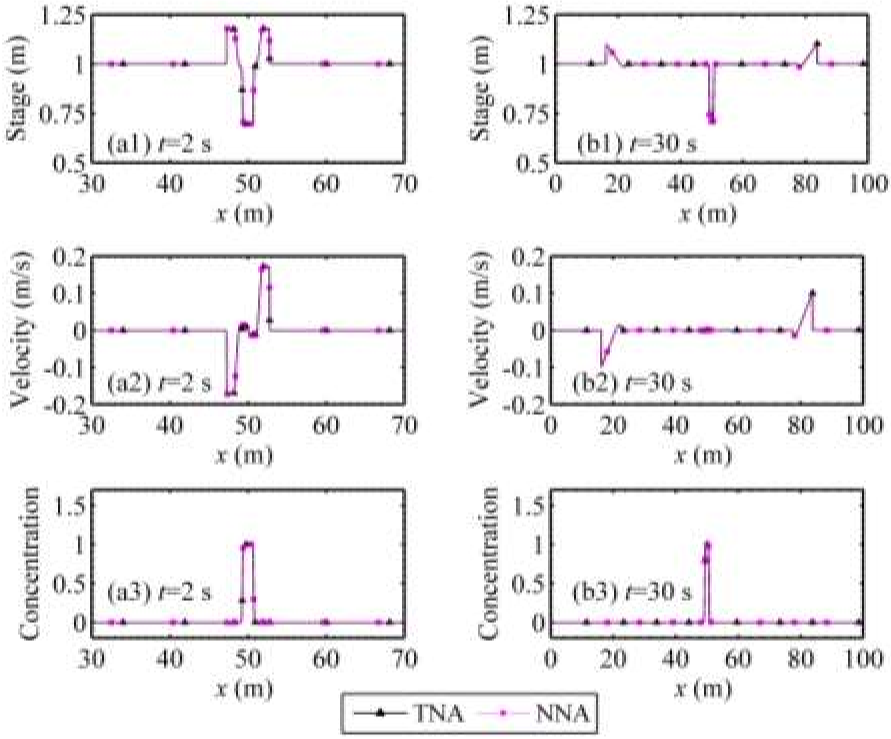

Figure 7. Case 3b: stage, velocity, and concentration profiles at times (a) $t = 2$ s and (b) $t = 30$ s, predicted by FCNA and CNA for density dam break ($\rho_{in} = 2.0$ kg/m^3) with two discontinuities.

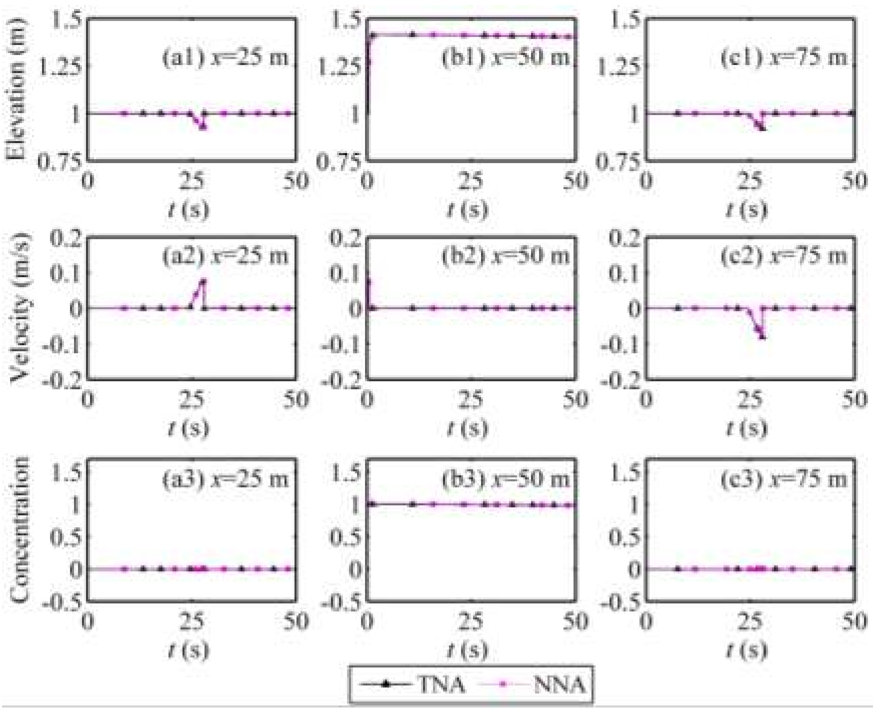

Figure 8. Case 3a: stage, velocity, and concentration time histories at locations (a) $x = 225$ m, and (b) $x = 275$ m, predicted by FCNA and CNA for density dam break ($\rho_{in} = 0.5$ kg/m^3) with two discontinuities.

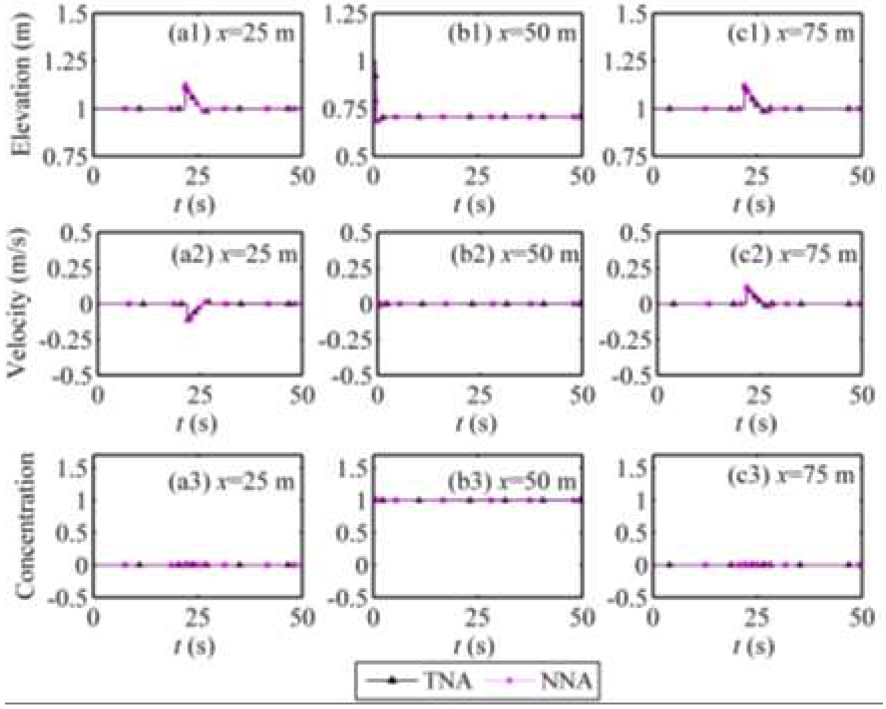

Figure 9. Case 3b: Stage, velocity, and concentration time histories at locations (a) $x = 225$ m, and (b) $x = 275$ m, predicted by FCNA and CNA for density dam break ($\rho_{in} = 2.0$ kg/m^3) with two discontinuities.

Table IV. L_{hz}, L_u and L_c for Case 3a (ρ_{in} = 0.5 kg/m^3)

Location or Time	$x = 25$ m	$x = 50$ m	$x = 75$ m	$t = 2$ s	$t = 30$ s
L_{hz} (%)	0.01	0.02	0.03	0.01	0.01
L_u (%)	0.69	N/A	0.56	3.79	2.19
L_c (%)	N/A	0.00	N/A	0.03	0.04

Table V. L_{hz}, L_u and L_c for Case 3b (ρ_{in} = 2.0 kg/m^3)

Location or Time	$x = 25$ m	$x = 50$ m	$x = 75$ m	$t = 2$ s	$t = 30$ s
L_{hz} (%)	0.02	0.03	0.02	0.01	0.03
L_u (%)	3.2	N/A	0.07	3.00	3.87
L_c (%)	N/A	0.00	N/A	0.27	0.02

3.4 Case 4: Dam-break over erodible beds of prototype scale

Case 4 is used to test the relative performance of FCNA and CNA in modelling the mobile bed hydraulics due to the instantaneous, full collapse of a dam. This test case was first proposed by Cao et al. (2004) for a dam break in a long channel at prototype scale, with the simulation being of relatively long duration. The dam is located at the centre of a 50-km-long channel. Initially, the bed is horizontal and the static water depths upstream and downstream of the dam are 40 m and 2 m respectively. The duration of the numerical simulations was such that they were concluded before forward and backward waves reached the downstream and upstream boundaries, so that the boundary conditions could be simply set according to the initial static states. The same empirical relationships are implemented for net sediment exchange flux as used by Cao et al. (2004).

Figure 10 compares longitudinal profiles of water surface, bed elevation, velocity and concentration predicted by FCNA and CNA at two times after the initial dam break event. Figure 11 illustrates the temporal variations of stage, bed elevation, velocity, and concentration at sections $x = 23$ and $x = 27$ km (i.e. 2 km upstream and downstream of the dam, respectively). It can be seen that FCNA and CNA both give very similar predictions of the dam break process as it evolves. Not only the location of the hydraulic jump ((a1) and (b1) in Fig. 10), but also the abrupt fall in the free surface due to the existence of the contact discontinuity of sediment concentration ((a3) and (b3) in Fig. 10) are properly modelled by the FCNA. It should be noted that the sharp concentration gradient at the wavefront ((a3) and (b3) in Fig. 10) is modelled by the second term of the second component of Eq. (6d) by the CNA, whereas it is incorporated in the mixture density variation term ρh by the FCNA. Table VI lists values of L_{hz}, L_z, L_u and L_c, which are within 0.5%, 1%, 1% and 1.5% respectively at the selected sections and instants, demonstrating that the discrepancies between the FCNA and CNA are hardly distinguishable.

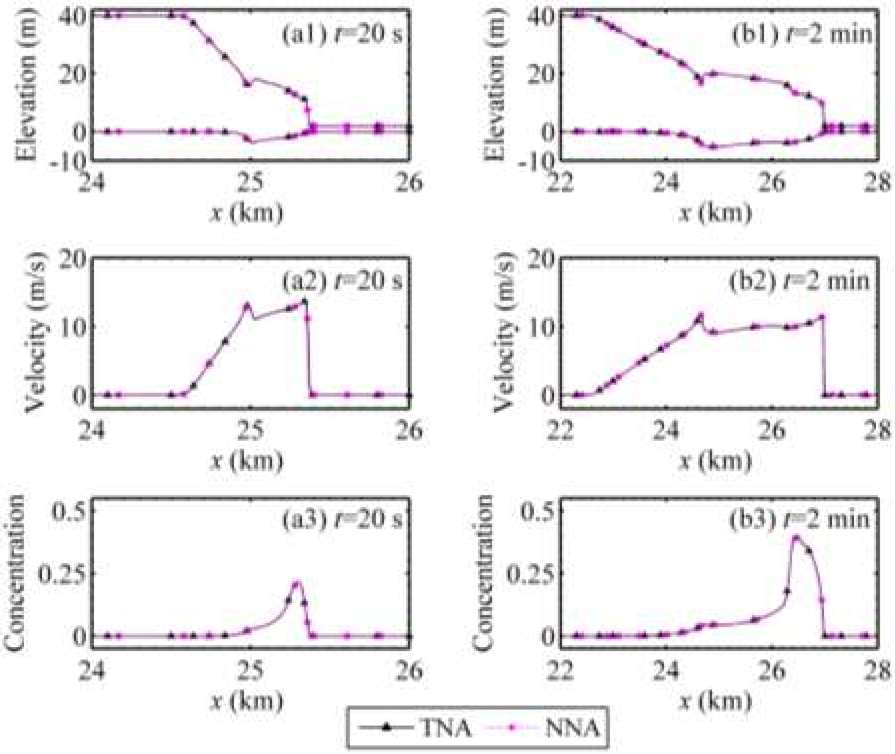

Figure 10. Case 4: dam break over an erodible bed at prototype scale: profiles of (a) water surface and bed elevation, (b) velocity, and (c) concentration predicted by FCNA and CNA at times $t = 20$ s and 2 min.

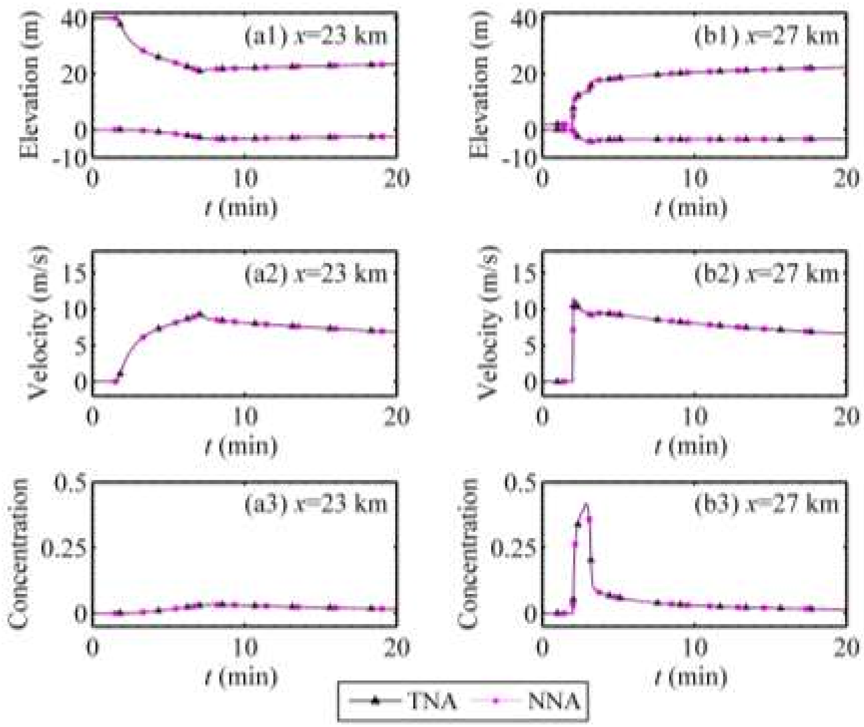

Figure 11. Case 4: dam break over an erodible bed at prototype scale: time histories of (a) water surface and bed elevation, (b) velocity, and (c) concentration predicted by FCNA and CNA at locations $x = 23$ km and 27 km.

Table VI. L_{hz}, L_z, L_u and L_c for Case 4

Location or Time	$x = 23$ km	$x = 27$ km	$t = 20$ s	$t = 2$ min
L_{hz} (%)	0.30	0.30	0.00	0.01
L_z (%)	0.30	0.54	0.76	0.43
L_u (%)	0.07	0.12	0.55	0.25
L_c (%)	0.25	0.48	1.47	0.73

3.5 Case 5: Experimental dam-break over erodible beds

Laboratory experiments of dam break flow over a mobile bed reported in the literature include those of Capart and Young 1998, Fraccarollo and Capart 2002, Spinewine and Zech 2007, and Zech et al. 2008. Case 5, considered here, is that of Fraccarollo and Capart (2002) who conducted dam break tests in a channel 2.5 m long, 0.1 m wide and 0.25 m deep. The initial static water depths upstream and downstream of the dam were 0.1 m and 0 m respectively. In the numerical models, the boundary conditions are set to be the same as for Case 4. The net sediment exchange flux is determined following Cao et al. (2011b) with modification coefficients $\beta = 9$ and $\varphi = 3$. Tables I and II list the remaining model parameters.

Figure 12 shows measured and predicted stage and bed elevation profiles along a 2.5 m reach of the channel at times $t = 0.505$ and 1.01 s after the dam break. Figure 13 displays the corresponding velocity and concentration profiles. The agreement between the FCNA and CNA simulations and the experimental measurements is fairly good; the initial bore and rarefaction waves match well, though there is some slight discrepancy between the measured and predicted reflected wave that seems trapped as a hydraulic jump at the location of the original dam break. This wave reflects from the bed as it is eroded, and its magnitude is underestimated by the FCNA and CNA numerical models (both of which give almost identical results). The velocity and concentration profiles are both characterized by an abrupt fall in velocity a sharp spike in concentration at the initial bore front as it propagates downstream. Figure 14 compares the FCNA and CNA predicted stage, bed elevation, velocity, and concentration time series at $x = -0.05$ and $x = 0.05$ m (0.05 m upstream and downstream of the initial dam respectively). The close agreement between the FCNA and CNA results is corroborated quantitatively in Table VII by the values of L_{hz}, L_z, L_u and L_c that are all within 1.5%. Meanwhile, the FCNA and CNA results both display similar differences to the measured stage (as mentioned above) leading to values of L^*_{hz} of 7.41% for FCNA and 7.38% for CNA at $t = 0.505$ s and 8.86% and 8.90% at $t = 1.01$ s, respectively. The results from Case 4 (involving large temporal and spatial scales) and Case 5 (involving experimental data at laboratory scale) help provide confidence in the FCNA as a model for highly unsteady shallow flows with shock waves and sediment transport.

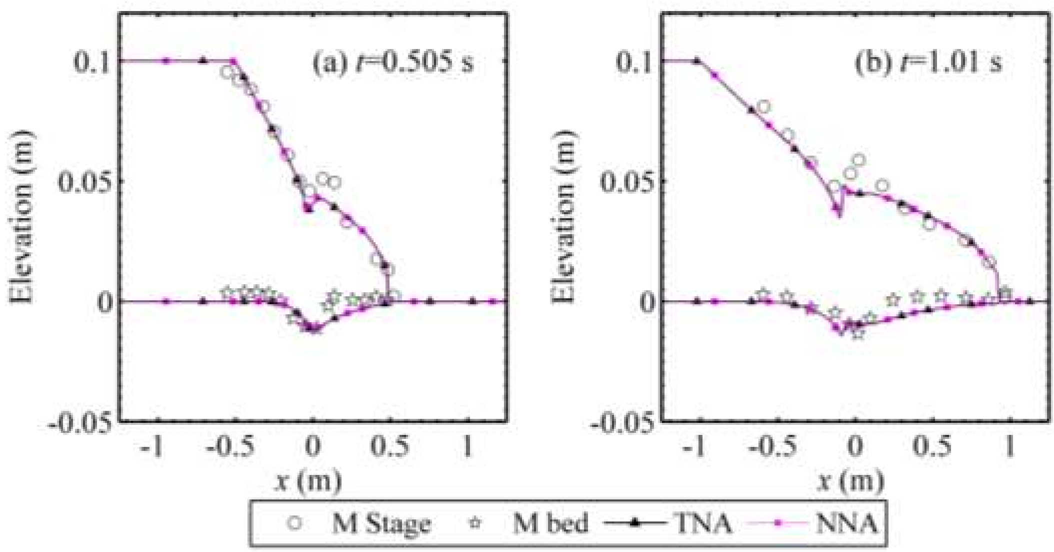

Figure 12. Case 5: computed (FCNA and CNA) and measured (Fraccarollo and Capart, 2002) water surface and bed elevation profiles at (a) $t = 0.505$ and (b) $t = 1.01$ s for a dam break over an erodible bed.

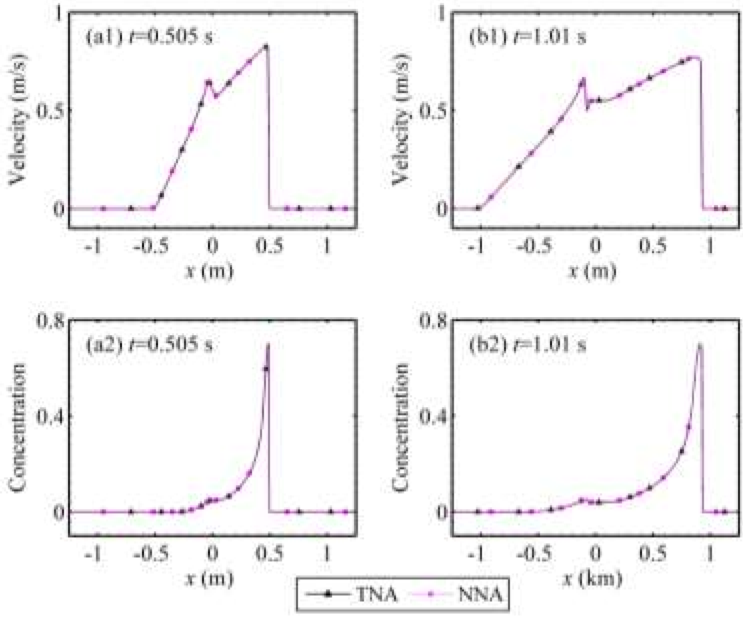

Figure 13. Case 5: computed (FCNA and CNA) and measured (Fraccarollo and Capart, 2002) water surface and bed elevation profiles at (a) $t = 0.505$ and (b) $t = 1.01$ s for a dam break over an erodible bed.

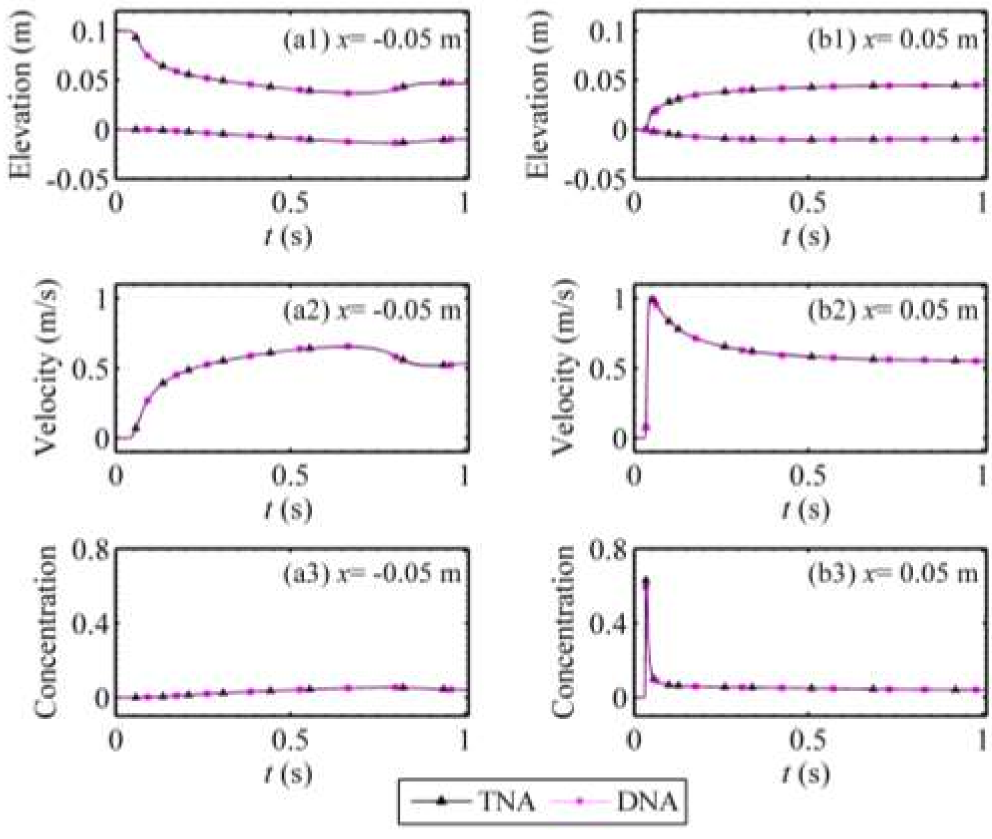

Figure 14. Case 5: computed (FCNA and CNA) and measured (Fraccarollo and Capart, 2002) water surface, bed elevation, velocity, and concentration time series at (a) $x = -0.05$ m and (b) $x = 0.05$ m for a dam break over an erodible bed.

Table VII. L_{hz}, L_z, L_u, L_c and L^*_{hz} for Case 5

Location or Time	x = -0.05 m	x = 0.05 m	t = 0.505 s	t = 1.01 s
L_{hz} (%)	0.92	0.92	0.34	0.10
L_z (%)	0.94	0.86	0.57	0.59
L_u (%)	0.43	0.38	0.13	0.19
L_c (%)	0.70	1.38	0.58	0.51
L^*_{hz} of FCNA (%)	N/A	N/A	7.41	8.86
L^*_{hz} of CNA (%)	N/A	N/A	7.38	8.90

3.6 Case 6: Flood flow due to landslide dam failure

Landslide dam failures involve wet-dry fronts propagating over irregular bed topography, and so constitute prime test cases by which to evaluate and compare the FCNA and CNA models in terms of their well-balanced properties and their treatment of wet-dry interfaces, in addition to shock capturing. Cao et al. (2011a) document results from a series of flume experiments on landslide dam breaches and subsequent flood wave propagation in a large-scale flume of dimensions 80 m × 1.2 m × 0.8 m and a fixed bed slope of 0.001. The experiments were implemented for different types of dams (i.e. with and without an initial breach) and dam material compositions in order to provide a unique, systematic set of measured data for validating numerical models of dam breaches and the resulting floods.

To demonstrate the performance of the FCNA, a uniform sediment case with no initial breach, i.e., F-case 15 (Cao et al. 2011a), is revisited here as Case 6. In this case, the dam was located at 41 m from the flume inlet, was 0.4 m high and had a crest width of 0.2 m. The initial upstream and downstream slopes of the dam were 1:4 and 1:5, respectively. The initial static water depths immediately upstream and downstream of the dam were 0.054 m and 0.048 m respectively. The inlet flow discharge was 0.025 m^3/s^{-1}, and no sediment was present. A 0.15 m high weir was situated at the outlet of the laboratory flume, and so a transmissive condition was imposed at the downstream boundary of the numerical models. Following Cao et al. (2011b), the net sediment exchange flux is determined with modification coefficients $\beta = 9$ and $\varphi = 3$ for both FCNA and CNA.

Figure 15 shows the predicted and measured stage hydrographs at selected cross sections. For F-case 15, cross-sections CS1 and CS5 are 22 m and 1 m upstream of the dam, whilst cross-sections CS8 and CS12 are 13 m and 32.5 m downstream of the dam. The stage hydrographs computed by FCNA and CNA are both in good agreement with the measured data from Cao et al. (2011a). Figure 16 presents the predicted water surface and bed profiles along with the measured stage at times t =670, 730 (shortly after the erosion of the dam) and 900 s (nearly final state of the dam failure). It is hard to say which algorithm better reproduces the processes of the dam failure as both the simulations of NNA and TNA match the measured data very well and the differences between the results of the two algorithms are too subtle to distinguish. Echoing Figs. 15 and 16, the values of the L_{hz}^{*} in Table VIII provide further insight into the relative performances of FCNA and CNA in comparison with the measured stage. The values of L_{hz}^{*} are around 1% at the selected sections but increase to around 8% at selected instants, which may be ascribed to the density of scattered measured data. However, the values of L_{hz}^{*} in Table VIII also demonstrate the stage is predicted by FCNA and CNA to almost the same accuracy, which further confirms that both algorithms can successfully deal with the complex flow and sediment transport processes associated with contact discontinuities as they propagate over irregular topographies.

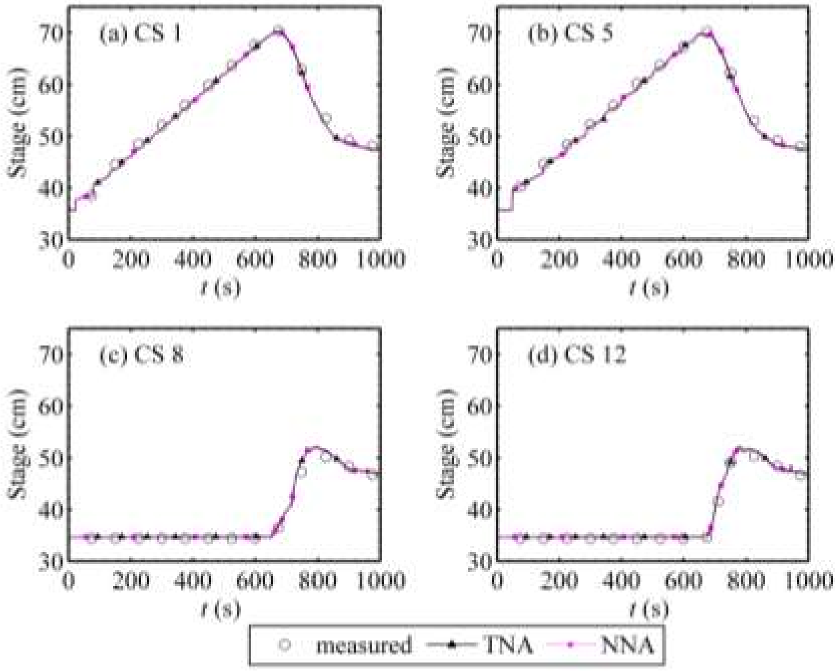

Figure 15. Case 6: predicted (FCNA and CNA) and measured (Cao et al. 2011a) stage hydrographs at four cross-sections for a channel flow induced by a landslide dam failure at laboratory-scale.

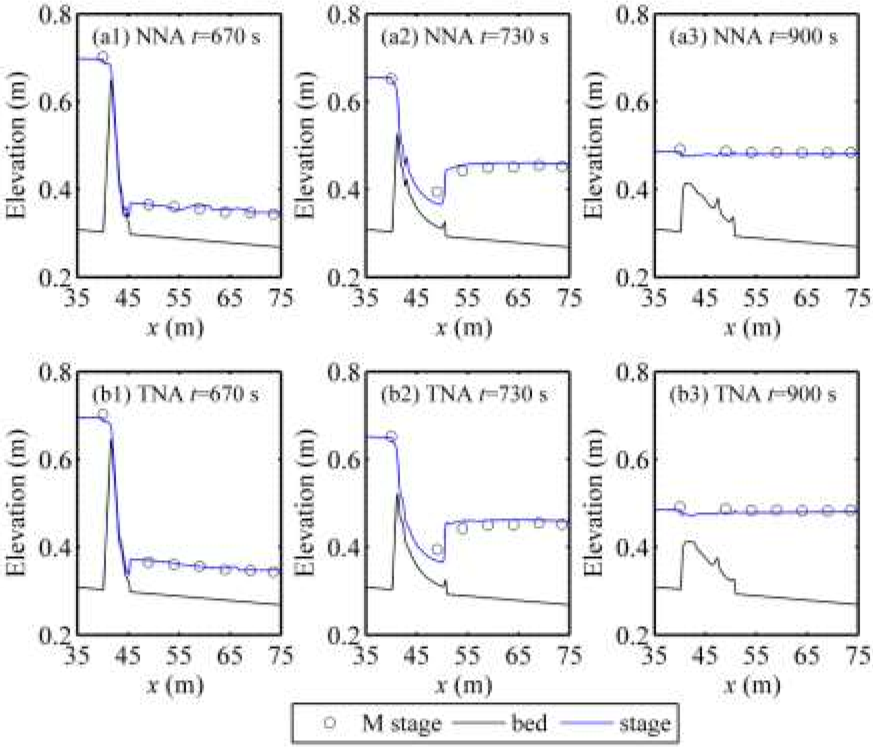

Figure 16. Case 6: predicted (FCNA and CNA) water surface and bed profiles, and measured stage profiles (Cao et al. 2011a), at times $t = 670$, 770 and 870 s for channel flow induced by a landslide dam failure at laboratory-scale.

Table VIII. L_{hz}^{*} for Case 6

Location or Time	CS 1	CS 5	CS 8	CS 12	$t = 670\,\text{s}$	$t = 730\,\text{s}$	$t = 900\,\text{s}$
L_{hz}^{*} of FCNA (%)	0.90	0.81	1.12	1.05	7.00	8.53	9.82
L_{hz}^{*} of CNA (%)	1.09	0.97	1.09	0.99	7.57	8.98	10.10

4. Conclusion

A numerical algorithm, FCNA, has been presented to solve the coupled SHSM equations directly, based on an unmodified full conservation form of the equations with mixture density maintained on the LHS of the equation set. When implemented with the well-balanced WSDGM version of the SLIC scheme, FCNA performed satisfactorily for the following series of test cases: steady equilibrium flow over a steep hump, density dam breaks with single and multiple discontinuities, dam breaks over erodible beds at prototype and laboratory scale, and a flood flow due to a landslide dam failure. It was demonstrated that the FCNA algorithm properly modelled complicated flows with sharp fronts (in stage and velocity), sediment transport processes with contact discontinuities over irregular topographies, and non-equilibrium bed morphological change. Moreover, it was found that the conventional CNA, based on redistribution of the water-sediment mixture density term, achieved very similar accuracy to the FCNA over the range of verification and validation tests considered. These findings indicate that both the FCNA and CNA algorithms can be satisfactorily applied in computational river modelling.

Acknowledgements

The work reported in this manuscript is funded by Natural Science Foundation of China (Grants No. 51279144 and 11432015).

References

Aureli, F., Maranzoni, A. and Mignosa, P. (2004), "Two dimensional modeling of rapidly varying flows by finite volume schemes", *River Flow*, pp. 837-847.

Aureli, F., Maranzoni, A., Mignosa, P. and Ziveri, C. (2008), "A weighted surface-depth gradient method for the numerical integration of the 2D shallow water equations with topography", *Advances in Water Resources*, Vol. 31 No. 7, pp. 962-974.

Batchelor, G. K. (1967), *An Introduction to Fluid Dynamics*, Cambridge University Press, England.

Bellos, C. V., Soulis, V. and Sakkas, J. G. (1992), "Experimental investigation of two-dimensional dam-break induced flows", *Journal of Hydraulic Research*, Vol. 30 No. 1, pp. 47-63.

Bermudez, A. and Vazquez, M. E. (1994), "Upwind methods for hyperbolic conservation laws with source terms", *Computers & Fluids*, Vol. 23 No. 8, pp. 1049-1071.

Cao, Z., Li, J., Pender, G. and Liu, Q. (2015), "Whole-Process Modeling of Reservoir Turbidity Currents by a Double layer-Averaged Model", *Journal of Hydraulic Engineering*, Vol. 141 No. 2, pp. 04014069.

Cao, Z., Pender, G., Wallis, S. and Carling, P. (2004), "Computational dam-break hydraulics over erodible sediment bed", *Journal of Hydraulic Engineering*, Vol. 130 No. 7, pp. 689-703.

Cao, Z., Yue, Z. and Pender, G. (2011a), "Landslide dam failure and flood hydraulics. Part I: experimental investigation", *Natural Hazards*, Vol. 59 No. 2, pp. 1003-1019.

Cao, Z., Yue, Z. and Pender, G. (2011b), "Landslide dam failure and flood hydraulics. Part II: coupled mathematical modelling", *Natural Hazards*, Vol. 59 No. 2, pp. 1021-1045.

Capart, H. and Young, D. L. (1998), "Formation of a jump by the dam-break wave over a granular bed", *Journal of Fluid Mechanics*, Vol. 372 No. 165-187.

Cea, L. and Vázquez-Cendón, M. E. (2010), "Unstructured finite volume discretization of two-dimensional depth-averaged shallow water equations with porosity", *International Journal for Numerical Methods in Fluids*, Vol. 63 No. 8, pp. 903-930.

Fraccarollo, L. and Capart, H. (2002), "Riemann wave description of erosional dam-break flows", *Journal of Fluid Mechanics*, Vol. 461, pp. 183-228.

Fraccarollo, L. and Toro, E. F. (1995), "Experimental and numerical assessment of the shallow water model for two-dimensional dam-break type problems", *Journal of Hydraulic Research*, Vol. 33 No. 6, pp. 843-864.

Gear, C. W. (1971), *Numerical Initial Value Problems in Ordinary Differential Equations*, Prentice Hall PTR Upper Saddle River, New Jersey, USA.

Gottlieb, S. and Shu, C. W. (1998), "Total variation diminishing Runge-Kutta schemes", *Mathematics of computation*, Vol. 67 No. 221, pp. 73-85.

Harten, A., Lax, P. D. and van Leer, B. (1983), "On upstream differencing and Godunov-type schemes for hyperbolic conservation laws", *SIAM Review*, Vol. 25 No. 1, pp. 35-61.

Hu, P. and Cao, Z. (2009), "Fully coupled mathematical modeling of turbidity currents over erodible bed", *Advances in Water Resources*, Vol. 32 No. 1, pp. 1-15.

Hu, P., Cao, Z., Pender, G. and Tan, G. (2012), "Numerical modelling of turbidity currents in the Xiaolangdi reservoir, Yellow River, China", *Journal of Hydrology*, Vol. 464-465 No. 0, pp. 41-53.

Hu, P., Li, W., He, Z., Päht, T. and Yue, Z. (2015), "Well-balanced and flexible morphological modeling of swash hydrodynamics and sediment transport", *Coastal Engineering*, Vol. 96, pp. 27-37.

Huang, W., Cao, Z., Carling, P. and Pender, G. (2014), "Coupled 2D Hydrodynamic and Sediment Transport Modeling of Megaflood due to Glacier Dam-break in Altai Mountains, Southern Siberia", *Journal of Mountain Science*, Vol. 11 No. 6, pp. 1442-1453.

Huang, W., Cao, Z., Yue, Z., Pender, G. and Zhou, J. (2012), "Coupled modelling of flood due to natural landslide dam breach", *Proceedings of the ICE - Water Management*, Vol. 165 No. 10, pp. 525-542.

Kim, D.-H. (2015), "H2D morphodynamic model considering wave, current and sediment interaction", *Coastal Engineering*, Vol. 95, pp. 20-34.

Kim, J., Ivanov, V. Y. and Katopodes, N. D. (2013), "Modeling erosion and sedimentation coupled with hydrological and overland flow processes at the watershed scale", *Water Resources Research*, Vol. 49 No. 9, pp. 5134-5154.

Leal, J. G. A. B., Ferreira, R. M. L. and Cardoso, A. H. (2006), "Dam-Break Wave-Front Celerity ", *Journal of Hydraulic Engineering*, Vol. 132 No. 1, pp. 69-76.

Leighton, F. Z., Borthwick, A. G. L. and Taylor, P. H. (2010), "1-D numerical modelling of shallow flows with variable horizontal density", *International Journal for Numerical Methods in Fluids*, Vol. 62 No. 11, pp. 1209-1231.

Li, S. and Duffy, C. J. (2011), "Fully coupled approach to modeling shallow water flow, sediment transport, and bed evolution in rivers", *Water Resources Research*, Vol. 47 No. 3, pp. 1-20.

Li, W., van Maren, D. S., Wang, Z. B., de Vriend, H. J. and Wu, B. (2014), "Peak discharge increase in hyperconcentrated floods", *Advances in Water Resources*, Vol. 67, pp. 65-77.

Liang, Q. and Borthwick, A. (2009), "Adaptive quadtree simulation of shallow flows with wet-dry fronts over complex topography", *Computers and Fluids*, Vol. 38 No. 2, pp. 221-234.

Liang, Q. and Marche, F. (2009), "Numerical resolution of well-balanced shallow water equations with complex source terms", *Advances in Water Resources*, Vol. 32 No. 6, pp. 873-884.

Liska, R. and Wendroff, B. (1998), "Composite Schemes for Conservation Laws", *SIAM J. Numer. Anal.*, Vol. 35 No. 6, pp. 2250-2271.

Qian, H., Cao, Z., Pender, G., LIu, H. and Hu, P. (2015), "Well-balanced numerical modelling of non-uniform sediment transport in alluvial rivers", *International Journal of Sediment Research*, Vol. 30 No. 2, pp. 117-130.

Roe, P. L. (1981), "Approximate Riemann Solvers, Parameter Vectors and Difference Schemes", *Journal of computational physics*, Vol. 43 No. 2, pp. 357-372.

Rogers, B. D., Borthwick, A. G. L. and Taylor, P. H. (2003), "Mathematical balancing of flux gradient and source terms prior to using Roe's approximate Riemann solver", *Journal of Computational Physics*, Vol. 192 No. 2, pp. 422-451.

Simpson, G. and Castelltort, S. (2006), "Coupled model of surface water flow, sediment transport and morphological evolution", *Computers & Geosciences*, Vol. 32 No. 10, pp. 1600-1614.

Spinewine, B. and Zech, Y. (2007), "Small-scale laboratory dam-break waves on movable beds", *Journal of Hydraulic Research*, Vol. 45 No. sup1, pp. 73-86.

Toro, E. F. (1999), *Riemann solvers and numerical methods for fluid dynamics*, Springer-Verlag, Germany.

Toro, E. F. (2001), *Shock-capturing methods for free-surface shallow flows*, John Wiley, England.

Toro, E. F., Spruce, M. and Speares, W. (1994), "Restoration of the contact surface in the HLL-Riemann solver", *Shock waves* Vol. 4, pp. 25-34.

Wu, W. (2007), *Computational river dynamics*, Taylor & Francis, London.

Wu, W., Marsooli, R. and He, Z. (2012), "Depth-averaged two-dimensional model of unsteady flow and sediment transport due to noncohesive embankment break/breaching", *Journal of Hydraulic*

Engineering, Vol. 138 No. 6, pp. 503-516.

Wu, W. and Wang, S. (2008), "One-dimensional explicit finite-volume model for sediment transport", *Journal of Hydraulic Research*, Vol. 46 No. 1, pp. 87-98.

Wu, W. and Wang, S. S. Y. (2007), "One-dimensional modeling of dam-break flow over movable beds", *Journal of Hydraulic Engineering*, Vol. 133 No. 1, pp. 48-58.

Xia, J., Lin, B., Falconer, R. A. and Wang, G. (2010), "Modelling dam-break flows over mobile beds using a 2D coupled approach", *Advances in Water Resources*, Vol. 33 No. 2, pp. 171-183.

Xiao, H., Young, Y. and Prévost, J. H. (2010), "Hydro- and morpho-dynamic modeling of breaking solitary waves over a fine sand beach.Part II: Numerical simulation", *Marine Geology*, Vol. 269 No. 3-4, pp. 107-118.

Xie, J. ed. (1990), *River Modelling*. China Water and Power Press, Beijing (in Chinese).

Yue, Z., Liu, H., Li, Y., Hu, P. and Zhang, Y. (2015), "A Well-Balanced and Fully Coupled Noncapacity Model for Dam-Break Flooding", *Mathematical Problems in Engineering*, Vol. 2015, pp. 1-13.

Yue, Z., Cao, Z., Li, X. and Che, T. (2008), "Two-dimensional coupled mathematical modeling of fluvial processes with intense sediment transport and rapid bed evolution", *Science in China Series G: Physics Mechanics and Astronomy*, Vol. 51 No. 9, pp. 1427-1438.

Zech, Y., Soares-Frazao, S., Spinewine, B. and Grelle, N. L. (2008), "Dam-break induced sediment movement: Experimental approaches and numerical modelling", *Journal of Hydraulic Research*, Vol. 46 No. 2, pp. 176-190.

Zhang, S. and Duan, J. G. (2011), "1D finite volume model of unsteady flow over mobile bed", *Journal of Hydrology*, Vol. 405 No. 1-2, pp. 57-68.

Zhou, J. G., Causon, D. M., Mingham, C. G. and Ingram, D. M. (2001), "The surface gradient method for the treatment of source terms in the shallow-water equations", *Journal of Computational Physics*, Vol. 168 No. 1, pp. 1-25.

Zhu, F. and Dodd, N. (2015), "The morphodynamics of a swash event on an erodible beach", *Journal of Fluid Mechanics*, Vol. 762, pp. 110-140.

Corresponding author

Professor Zhixian Cao can be contacted at: *zxcao@whu.edu.cn*

List of Tables

Table I. Spatial increment and Courant number used in test cases

Test case	1	2	3	4	5	6
Spatial step Δx (m)	0.05	0.02	0.02	10	0.005	0.04
Courant number C_r	0.95	0.95	0.95	0.95	0.95	0.95

Table II. Summary of test cases

Test case	Sediment density ρ_s (kg/m^3)	Water density ρ_w (kg/m^3)	Gravitational acceleration g (m/s^2)	Sediment diameter d (mm)	Manning roughness n	Sediment porosity p
1	2,650	1,000	9.8	N/A	0.0	N/A
2	10.0	1.0	1.0	N/A	0.0	N/A
3	0.5&2.0	1.0	1.0	N/A	0.0	N/A
4	2,650	1,000	9.8	8.0	0.03	0.4
5*	1,540	1,000	9.8	3.5	0.025	0.3
6*	2,650	1,000	9.8	0.8	0.012	0.4

Notes: * Cases using measured data.

Table III. L_{hz}, L_u and L_c for Case 2

Location or Time	$x = 225$ m	$x = 275$ m	$t = 30$ s	$t = 100$ s
L_{hz} (%)	0.01	2.24	0.30	0.68
L_u (%)	0.02	2.07	2.92	1.95
L_c (%)	0.00	1.93	0.17	0.33

Table IV. L_{hz}, L_u and L_c for Case 3a (ρ_{in} = 0.5 kg/m^3)

Location or Time	$x=25$ m	$x=$ 50 m	$x=$ 75 m	$t=2$ s	$t=30$ s
L_{hz} (%)	0.01	0.02	0.03	0.01	0.01
L_u (%)	0.69	N/A	0.56	3.79	2.19
L_c (%)	N/A	0.00	N/A	0.03	0.04

Table V. L_{hz}, L_u and L_c of Case 3b (ρ_{in} = 2.0 kg/m^3)

Location or Time	$x=25$ m	$x=$ 50 m	$x=$ 75 m	$t=2$ s	$t=30$ s
L_{hz} (%)	0.02	0.03	0.02	0.01	0.03
L_u (%)	3.2	N/A	0.07	3.00	3.87
L_c (%)	N/A	0.00	N/A	0.27	0.02

Table VI. L_{hz}, L_z, L_u and L_c for Case 4

Location or Time	$x=23$ km	$x=$ 27 km	$t=20$ s	$t=2$ min
L_{hz} (%)	0.30	0.30	0.00	0.01
L_z (%)	0.30	0.54	0.76	0.43
L_u (%)	0.07	0.12	0.55	0.25
L_c (%)	0.25	0.48	1.47	0.73

Table VII. L_{hz}, L_z, L_u, L_c and L_{hz}^* for Case 5

Location or Time	$x = -0.05$ m	$x = 0.05$ m	$t = 0.505$ s	$t = 1.01$ s
L_{hz} (%)	0.92	0.92	0.34	0.10
L_z (%)	0.94	0.86	0.57	0.59
L_u (%)	0.43	0.38	0.13	0.19
L_c (%)	0.70	1.38	0.58	0.51
L_{hz}^* of FCNA (%)	N/A	N/A	7.41	8.86
L_{hz}^* of CNA (%)	N/A	N/A	7.38	8.90

Table VIII. L_{hz}^* for Case 6

Location or Time	CS 1	CS 5	CS 8	CS 12	$t = 670$ s	$t = 730$ s	$t = 900$ s
L_{hz}^* of FCNA (%)	0.90	0.81	1.12	1.05	7.00	8.53	9.82
L_{hz}^* of CNA (%)	1.09	0.97	1.09	0.99	7.57	8.98	10.10

List of figure captions

Figure 1. Sketch of the WSDGM version of the SLIC scheme

Figure 2. Case 1a: equilibrium stage and velocity profiles predicted by FCNA and CNA for initial stage of 1.0 m

Figure 3. Case 1b: equilibrium stage and velocity profiles predicted by FCNA and CNA for initial stage of 0.5 m

Figure 4. Case 2: stage and velocity profiles predicted by FCNA and CNA for density dam break with a single discontinuity at times: (a) t = 30 s; and (b) t = 100s.

Figure 5. Case 2: stage and velocity time histories predicted by FCNA and CNA for density dam break with a single discontinuity at locations: (a) x = 225 m; and (b) x = 275 m.

Figure 6. Case 3a: stage, velocity, and concentration profiles at times (a) t = 2 s and (b) t = 30 s, predicted by FCNA and CNA for density dam break (ρ_{in} = 0.5 kg/m^3) with two discontinuities.

Figure 7. Case 3b: stage, velocity, and concentration profiles at times (a) t = 2 s and (b) t = 30 s, predicted by FCNA and CNA for density dam break (ρ_{in} = 2.0 kg/m^3) with two discontinuities.

Figure 8. Case 3a: stage, velocity, and concentration time histories at locations (a) x = 225 m, and (b) x = 275 m, predicted by FCNA and CNA for density dam break (ρ_{in} = 0.5 kg/m^3) with two discontinuities.

Figure 9. Case 3b: Stage, velocity, and concentration time histories at locations (a) x = 225 m, and (b) x = 275 m, predicted by FCNA and CNA for density dam break (ρ_{in} = 2.0 kg/m^3) with two discontinuities.

Figure 10. Case 4: dam break over an erodible bed at prototype scale: profiles of (a) water surface and bed elevation, (b) velocity, and (c) concentration predicted by FCNA and CNA at times t = 20 s and 2 min.

Figure 11. Case 4: dam break over an erodible bed at prototype scale: time histories of (a) water surface and bed elevation, (b) velocity, and (c) concentration predicted by FCNA and CNA at locations x = 23 km and 27 km.

Figure 12. Case 5: computed (FCNA and CNA) and measured (Fraccarollo and Capart, 2002) water surface and bed elevation profiles at (a) t = 0.505 and (b) t = 1.01 s for a dam break over an erodible bed.

Figure 13. Case 5: computed (FCNA and CNA) and measured (Fraccarollo and Capart, 2002) water surface and bed elevation profiles at (a) t = 0.505 and (b) t = 1.01 s for a dam break over an erodible bed.

Figure 14. Case 5: computed (FCNA and CNA) and measured (Fraccarollo and Capart, 2002) water surface, bed elevation, velocity, and concentration time series at (a) $x = -0.05$ m and (b) $x = 0.05$ m for a dam break over an erodible bed.

Figure 15. Case 6: predicted (FCNA and CNA) and measured (Cao et al. 2011a) stage hydrographs at four cross-sections for a channel flow induced by a landslide dam failure at laboratory-scale.

Figure 16. Case 6: predicted (FCNA and CNA) water surface and bed profiles, and measured stage profiles (Cao et al. 2011a), at times $t = 670$, 770 and 870 s for channel flow induced by a landslide dam failure at laboratory-scale.